Naval Research Laboratory
Washington, DC 20375-5320

NRL/MR/6791--15-9634

xLIPA: Promotion of Electrons from the K-shell to 2 GeV using 10 PW Laser Pulses

D.F. Gordon
J.P. Palastro
B. Hafizi
D. Kaganovich
L. Johnson
R. Hubbard
M.H. Helle
A. Ting

Beam Physics Branch
Plasma Physics Division

Y. Chen

Research Support Instruments, Inc.
Lanham, Maryland

August 19, 2015

xLIPA : Promotion of electrons from the K-shell to 2 GeV using 10 PW laser pulses

D.F. Gordon, J.P. Palastro, B. Hafizi, D. Kaganovich,

L. Johnson, R.F. Hubbard, M.H. Helle, and A. Ting

Beam Physics Branch, Plasma Physics Division

Y.-H. Chen

Research Support Instruments, Lanham, MD 20706

Inner shell atomic electrons that are tunnel ionized in multi-petawatt class laser pulses are accelerated, in vacuum, to multi-GeV energies in the forward direction. In extreme fields, tunnel ionized electrons can be brought to the speed of light so abruptly, that they stay in the same phase of the laser field throughout significant portions of the confocal region. An analysis of the acceleration process is given, and relativistically covariant four-dimensional numerical calculations especially suited for extreme fields are carried out. Radiation reaction is included, and the latest relativistic tunneling ionization theories are used to spawn the simulated electrons. An experimental configuration is suggested, utilizing the 10 petawatt ELI-NP laser, and plasma lens assisted focusing.

Manuscript approved July 17, 2015

Contents

I. Introduction 1

II. Analysis of the Ultra-relativistic Case 3

III. Numerical Simulations 5

A. Choice of Ionic Species and Ionization Thresholds 6

B. Electron Distributions at muliti-Petawatt Scale 9

C. Electron Distributions at multi-Exawatt Scale 11

D. Radiation Reaction 12

IV. Numerical Methods 14

A. Covariant Particle Pusher 15

B. Timestep Adjustment, Accuracy and Performance 17

C. Radiation Reaction 20

D. Ionization Algorithm 21

V. Nonlinear Propagation in a Plasma Lens 22

VI. Relativistic Ionization Theories 26

A. Critique of Analytical Approaches 27

1. Quasi-classicality 27

2. Gauge 28

3. Nuclear Coulomb Tail 28

B. Ab Initio Simulations 28

VII. Conclusions 29

VIII. Acknowledgements 29

References 31

I. INTRODUCTION

This report concerns a mechanism of electron acceleration by free space electromagnetic fields, wherein the electrons are supplied by the inner shell orbitals of moderately heavy atoms. The process involves both relativistic tunneling ionization, and classical charged particle dynamics in ultrarelativistic fields. With the imminent commissioning of the 10 petawatt (PW) beamlines at the ELI-NP facility [1], the proposed scheme promises to advance the state of the art of free space acceleration of electrons by about 3 orders of magnitude.

Acceleration of electrons by electromagnetic fields in free space has been investigated at length over the years [2–8]. Free space acceleration is usefully framed in terms of the Lawson-Woodward (LW) theorem [9], which, roughly speaking, states that upon linearizing the forces, the net energy gain is zero. Conventional accelerators overcome LW by introducing a metallic structure comparable in dimension to the wavelength of the electromagnetic field. Schemes such as the inverse Cherenkov accelerator [2] overcome LW by performing the acceleration in a gaseous medium (i.e., not in free space). Several schemes rely on the ponderomotive force to supply a nonlinearity which overcomes LW [3, 5, 7]. In the case of Laser Ionization and Ponderomotive Acceleration (LIPA) [5], an additional consideration is that tunnel-ionized electrons are introduced into the high-field region abruptly, further stressing the assumptions of LW. In the ultrarelativistic limit, the nonlinear forces cannot be described ponderomotively, because of the possibility of a slow rate of phase slippage. This is the basis of the "Capture and Accelerate Scenario" (CAS) [6], for which there is recent experimental evidence [8].

This report analyzes and simulates LIPA in extreme fields (xLIPA). In the original LIPA scheme, electrons originate from a tenuous gas of moderately heavy elements. Upon focusing a high-intensity laser pulse into the gas, electrons are tunnel ionized and accelerated. It is desirable in the LIPA scheme for the ionization potential to be matched to the laser power and focusing such that the electrons are ionized only when they are exposed to the peak laser intensity. Such electrons experience the highest ponderomotive potential, and therefore gain the greatest energy (electrons ionized earlier in the pulse may be pushed out of the focus before the peak of the pulse arrives). In the case of xLIPA, the ionization potential has to be matched in a similar way, but the acceleration is no longer ponderomotive. Instead,

electrons stripped from atoms with certain favorable initial positions are brought abruptly to the speed of light and gain further energy as they stay in nearly the same phase of the laser field for extended periods of time. This is essentially the acceleration mechanism of CAS, except that the electrons are bound to a parent ion, and hence nearly immobile, until the most intense portion of the laser pulses passes by. In practical terms, xLIPA accesses the CAS regime without the need for a source of externally injected electrons, which is a significant experimental advantage.

A schematic of the proposed experimental configuration is shown in Fig. 1. In considering a 10 PW laser system, one confronts the practical issue that the final focusing optic is likely to be a large, one-of-a-kind parabolic mirror, fixing the f-number for all experiments. To increase the flexibility of the apparatus, a plasma lens [10–13] can be introduced. The plasma lens can be positioned in regions where the laser intensity is high, and so does not have to be particularly large. In fact, in the case of xLIPA, the plasma lens itself can provide the ions from which electrons are stripped and accelerated. In particular, the parameters can be arranged so that the beam waist occurs near the back surface of the lens, where a tenuous plasma of partially ionized gas (say, argon) awaits further ionization by the focused laser pulse. For sufficient focusing strength, the K-shell electrons are tunnel ionized and brought to GeV energies. Apart from flexibility, the plasma lens offers three additional benefits. First, it is likely that a plasma lens target counteracts the tendency of pre-pulses to increase the waist size of the main pulse. Second, the plasma lens acts as an axially extended target

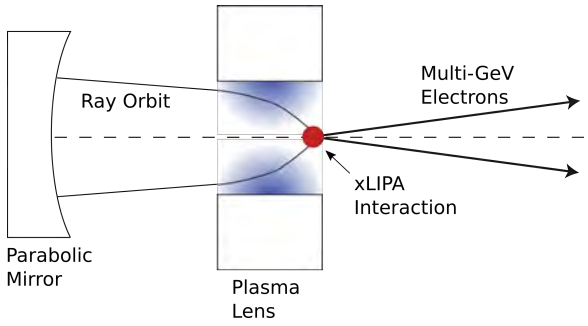

FIG. 1: Schematic xLIPA Configuration. The plasma lens is both the final focusing element and the target. It serves to (i) provide flexibility in focusing conditions, (ii) decrease sensitivity to pre-pulses and pointing stability, and (iii) provide an optimal configuration of ions from which xLIPA electrons are extracted.

with focusing properties throughout, which reduces sensitivity to errors in the position of the vacuum focus. Finally, as will be seen below, the highest energy xLIPA electrons originate off-axis, and therefore a target with an on-axis density minimum leads to a more favorable final energy distribution.

II. ANALYSIS OF THE ULTRA-RELATIVISTIC CASE

There is an exact solution for the motion of a charged particle in any radiation field of the form $F_{\mu\nu}(k_\mu x^\mu)$, where k_μ is the four dimensional wavevector of the radiation, and x_μ is the spacetime coordinate. Without loss of generality, let $k_1 = k_2 = 0$. Then $u_0 - u_3$ is invariant, where u_μ is the four dimensional velocity of the particle[1]. Combining this with the identity $u_\mu u^\mu = 1$, one can show that in the high energy limit $u_3 \gg \{u_1, u_2\}$. In other words, the particle moves predominatly in the "forward" direction, i.e., parallel to the radiation wavevector.

The following analysis is based on the expectation that in extreme laser fields, an inner shell electron that is tunnel-ionized, is accelerated abruptly to the speed of light. Then, according to the foregoing discussion, the direction of motion is nearly parallel to the wavevector of the radiation, and the phase of the particle in the radiation field can be regarded as constant. The primary constraint is that the interaction is limited to regions where the irradiance is high and the phase velocity is close to c. This corresponds to the two regions just outside the confocal region. That is, far from the confocal region the irradiance is too low, but inside the confocal region the phase velocity is too high.

The exact equations of motion for a particle in a plane wave, written as matrix equations, are

$$\frac{dx}{ds} = cu \tag{1}$$

$$\frac{du}{ds} = \Omega u \tag{2}$$

Here, $x(s)$ is the world line of the particle, $u(s)$ is the four-velocity, and $\Omega = a(s)\omega F$. The parameter s is the proper time, $a(s) = qE(s)/mc\omega$, $E(s)$ is the electric field, q is the charge of the particle, m is the mass, and ω is the frequency of the radiation. Using the coordinate

[1] In particular, $u = (\gamma, \gamma\beta_1, \gamma\beta_2, \gamma\beta_3)$, where $c\beta_i$ are the components of the three dimensional velocity, and $\gamma = (1 - \beta^2)^{-1/2}$

system described above, the matrix F is

$$F = \begin{pmatrix} 0 & 1 & 0 & 0 \\ 1 & 0 & 0 & -1 \\ 0 & 0 & 0 & 0 \\ 0 & 1 & 0 & 0 \end{pmatrix} \tag{3}$$

As long as the particle stays in phase, Ω can be regarded as constant, and the solution of the velocity equation is

$$u(s) = e^{\Omega s} u(0) \tag{4}$$

The matrix exponential $e^{\Omega s}$ is easily calculated due to the nilpotency of F, i.e., $F^3 = 0$. The result is

$$\Lambda(s) \equiv e^{\Omega s} = \begin{pmatrix} 1 + \sigma^2/2 & \sigma & 0 & -\sigma^2/2 \\ \sigma & 1 & 0 & -\sigma \\ 0 & 0 & 1 & 0 \\ \sigma^2/2 & \sigma & 0 & 1 - \sigma^2/2 \end{pmatrix} \tag{5}$$

where $\sigma(s) = a\omega s$. It is easily verified that Λ is a Lorentz transformation, i.e., $\Lambda^T g \Lambda = g$, where T indicates the transpose, and $g = \mathrm{diag}(1, -1, -1, -1)$. Of particular interest is the initial condition $u(0) = (1, 0, 0, 0)^T$, which according to most theories holds for an electron at the moment of ionization, at least when the atomic number satisfies $Z \ll 137$. In this case,

$$u(s) = \begin{pmatrix} 1 + \sigma^2/2 \\ \sigma \\ 0 \\ \sigma^2/2 \end{pmatrix} \tag{6}$$

Note that the invariant $u_0 - u_3$ is maintained. Moreover, when $\sigma = a\omega s \gg 1$ the momentum is predominantly in the forward direction, i.e., $u_3 \gg u_1$. Assuming $a \gg 1$, this requires that ωs be at least of order unity, i.e., the time elapsed according to a clock moving with the particle should read at least one laser period, as measured by a lab frame clock. This does not necessarily violate the assumption that the particle should stay in phase, since the two clocks may keep very different time.

Since the Rayleigh length characterizes the interaction length, which is expressed in terms

of x_3, it is useful to put s in terms of x_3. These are related by

$$x_3 = c\int u_3(s)ds = \frac{c}{6}a^2\omega^2 s^3 \tag{7}$$

Defining $k = \omega/c$ gives

$$s = \frac{(6x_3)^{1/3}}{c(ak)^{2/3}} \tag{8}$$

Then the energy of the particle is

$$u_0(x_3) = 1 + \frac{1}{2}\left(6akx_3\right)^{2/3} \tag{9}$$

Here, it is understood that the spacetime origin is chosen so that $x_3 = 0$ at the moment of ionization. Finally, the highest possible energy is estimated by substituting the Rayleigh length for x_3, i.e., $x_3 \to \pi r_0^2/\lambda$, where r_0 is the radius of the beam waist, and $\lambda = 2\pi/k$. This gives

$$u_{0,\max} = 1 + \frac{1}{2}\left(\frac{\pi r_0}{\lambda}\right)^{4/3}(12a)^{2/3} \tag{10}$$

or

$$u_{0,\max} \approx 12\left(\frac{r_0}{\lambda}\right)^{4/3} a^{2/3} \tag{11}$$

As an example, a 10 PW laser pulse, with $\lambda = 0.8$ μm, focused to $r_0 = 5$ μm, gives $a \approx 100$, and $u_{0,\max}mc^2 \approx 1.5$ GeV. The question of how to match the ionization potential of the ion to the laser parameters, so that the electron becomes free at the optimal time, is addressed below.

III. NUMERICAL SIMULATIONS

The primary observable in an xLIPA configuration is the electron momentum distribution. Under the assumption that the electrons are drawn from a gas whose density is low enough so that plasma effects are negligible, the momentum distribution can be obtained by single particle tracking methods. In the case of extreme fields, obtaining an accurate numerical solution to the equation of motion is non-trivial. The methods used in this work are detailed in section IV. In addition to integrating the equation of motion, the calculation has to account for tunneling ionization. For this purpose, an analytical rate law is needed. In this work, the Coulomb-corrected, dressed strong field approximation (SFA) of Klaiber et al. [14] is used. The particle tracking code used here also allows the exact Landau and Lifshitz

radiation reaction formula to be incorporated into the integration. It is found that at the 10 PW level this effect is very minor. An example based on more speculative laser parameters is given where the effect is noticeable.

A. Choice of Ionic Species and Ionization Thresholds

As is well known, the rate of tunneling ionization as a function of the electric field is exponential, so that the concept of a threshold field is applicable. The threshold for a given ionization potential determines where in the laser focus a free electron first appears. The ionization potential that leads to the highest energy electrons has to be calculated by performing a series of numerical experiments for a given laser power and focusing configuration. One expects that there is a finite optimum, for a threshold that is too high restricts the starting coordinate to a small region near the focus, while one that is too low restricts the starting coordinate to a region far from the focus, where the fields are too small to accelerate electrons in the forward direction before ejecting them radially.

One useful estimate for the threshold field is the one due to Augst [15], which is based on a simple barrier suppression picture, and is in reasonable agreement with experimental data. An alternative threshold based on the relativistic, Coulomb-corrected SFA (or any rate law) can be derived as follows. Let the rate be given as some function $w(U_i, E_0)$, where U_i is the ionization potential, and E_0 is the peak electric field of the applied laser pulse. The threshold field is that value of E_0 which satisfies $w(U_i, E_0) = \omega/2\pi$, where ω is the laser frequency. Note that since the dependence of the left hand side on E_0 is generally exponential, the result only depends logarithmically on the choice of time scale appearing on the right hand side.

Ionization thresholds for various ions are displayed in Table I based on the dressed Coulomb-corrected SFA [14]. The charge states displayed are selected based on their status as the highest charge states for a given set of non-empty shells, e.g., Ar^{7+} is the highest argon charge state that still has an electron in the M shell. When the atom is first exposed to the laser radiation, electrons are expected to be stripped sequentially, in order of increasing ionization potential. Therefore the potentials used at each stage are assumed to be those appropriate for an ion in the lowest energy state. It should be noted that the SFA rate law is strictly valid only for hydrogen-like ions. In addition to the intensity threshold, the

TABLE I: Tunneling Ionization Threshold for Ions of Interest

Ion	Potential (eV)	Occ. Shells	SFA Threshold[a] (W/cm^2)	a_0^{thresh} ($\lambda = 800$ nm)
Ar^{7+}	143	KLM	1.4×10^{17}	0.26
Ar^{15+}	918	KL	2.7×10^{19}	3.57
Ar^{17+}	4426	K	2.4×10^{21}	33.6
Ti^{21+}	6628	K	7.6×10^{21}	59.8
Fe^{25+}	9278	K	2.0×10^{22}	96.9
Kr^{35+}	17948	K	1.3×10^{23}	250
Xe^{53+}	41347	K	1.5×10^{24}	834
Au^{78+}	93459	K	1.6×10^{25}	2740
U^{91+}	132280	K	4.5×10^{25}	4570

[a]The static field rate is used to estimate the threshold. Cycle averaging increases the threshold by $\approx 25\%$.

corresponding peak normalized vector potential, a_0, is displayed. The parameter a_0 is of fundamental importance because the interaction becomes ultra-relativistic when $a_0 \gg 1$.

The laser pulse format assumed throughout section III is a waist radius ($1/e$ of the field) of 5 μm, a pulse length ($1/e$ of the field) of 20 fs, a wavelength of 0.8 μm, and a field configuration consistent with the lowest order Hermite-Gaussian mode. Longitudinal field components are chosen to be consistent with the Coulomb gauge ($\nabla \cdot \mathbf{A} = 0$), including a correction to account for finite pulse length. Two laser powers of primary interest are considered: 10 PW giving $a_0 = 100$, and 25 exawatts (EW) giving $a_0 = 5000$. The latter stupendous laser power is chosen because it gives a remarkable signature of radiation reaction. The former is chosen because it corresponds to the near-term ELI-NP parameters.

The effect of the ionization potential on the xLIPA distribution for the 10 PW case is shown in Fig. 2. The ionization potentials used correspond to 5 different ionic species, Ar^{7+}, Ar^{15+}, Ar^{17+}, Ti^{21+}, and Fe^{25+}. The latter three ions are all hydrogen-like. Representative particle orbits from the 5 cases are shown in Fig. 2(a), in the plane of energy and the longitudinal coordinate, x_3. The coordinate is raised to the 1/3 power in order to achieve the

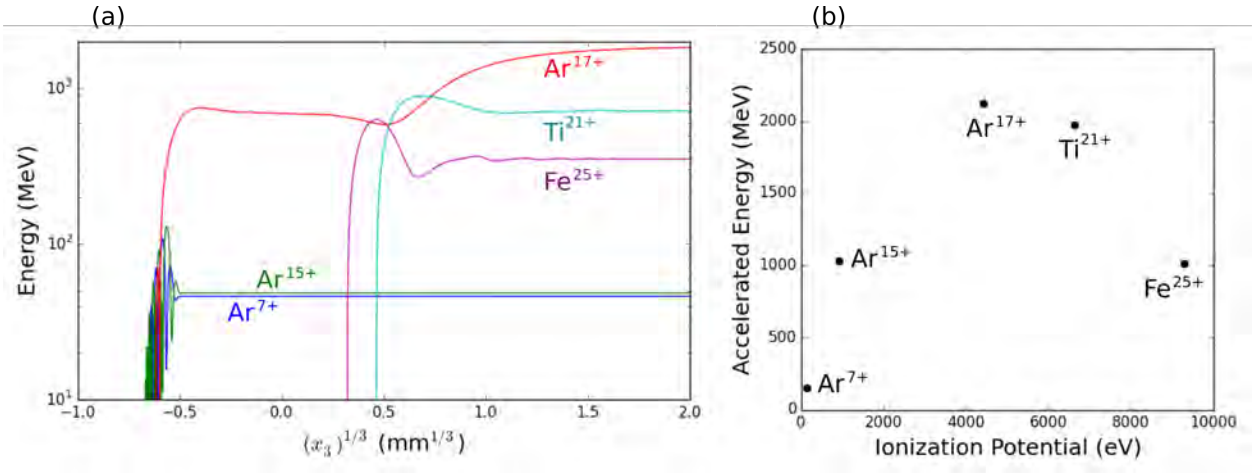

FIG. 2: Effect of ionization potential on electron acceleration for $a_0 = 100$. Representative orbits for ionization of 5 different ionic species are shown in (a), while the highest energy selected from an initial distribution of 10^6 particles is shown in (b) as a function of ionization potential, for the same 5 species.

effect of a logarithmic plot, while still allowing for a sign and a zero-crossing[2]. The lowest two charge states, with the smallest ionization potentials, are seen to experience ponderomotive acceleration, evidenced by the fast oscillations in energy superimposed on the overall energy gain. The net energy gain is also much smaller than that of the higher charge states, and the acceleration is terminated due to radial expulsion from the confocal region (not shown). In contrast the three higher charge state species exhibit a large energy gain within a single optical cycle, as evidenced by a steep initial slope devoid of any oscillatory features.

The anticipated peak in the maximum accelerated energy vs. ionization potential is illustrated in Fig. 2(b). In order to produce the data, 10^6 particles are loaded into a uniform distribution in a region sufficiently large to encompass the ionized volume. The particle with the highest energy, evaluated far from the laser focus, is used to define the maximum accelerated energy. In the case $a_0 = 100$, with the assumed focusing conditions, hydrogen-like argon turns out to be an optimal species.

[2] Strictly this requires the ad-hoc relationship $(-|x|)^{1/3} = -|x|^{1/3}$

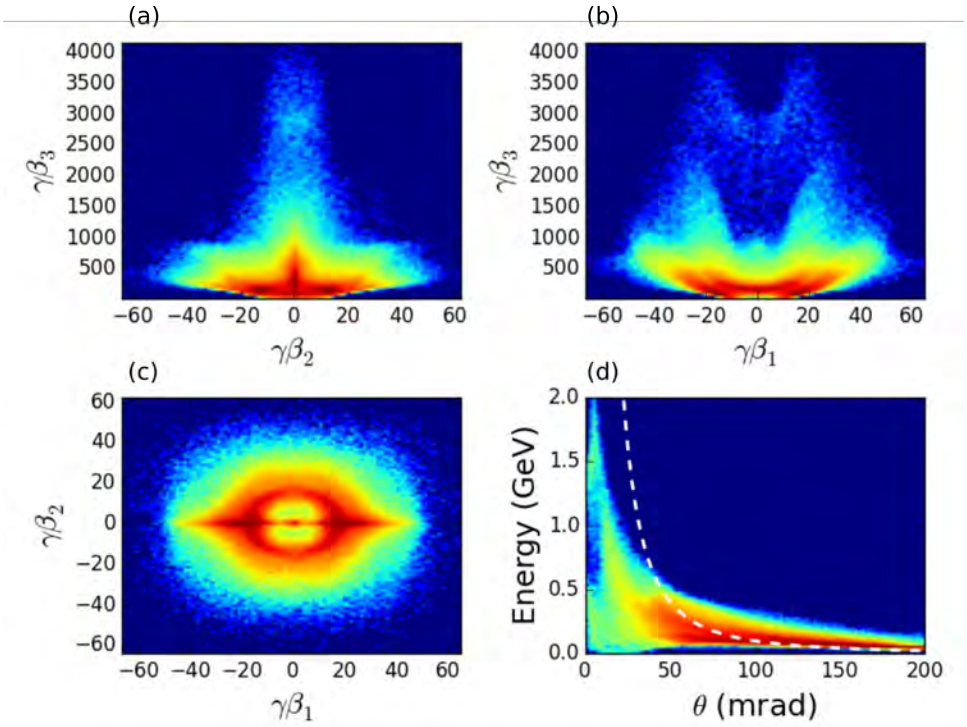

FIG. 3: Final distribution of electrons drawn from the K-shell of argon with 10 PW of laser power. The momentum space distribution is shown in (a,b,c), and the angular-spectral distribution is shown in (d). $\gamma\beta_i$ is momentum normalized to mc, with laser polarization in the 1-direction and central wavevector in the 3-direction. The color scale is logarithmic. The dashed line in (d) is the curve on which all particles would lie in the plane-wave limit.

B. Electron Distributions at muliti-Petawatt Scale

Based on the forgoing discussion, the ions Ar^{16+} and Ar^{17+} (both with similar ionization potentials) are of interest in terms of possible near-term ELI-NP experiments utilizing the 10 PW beamlines. In order to broadly characterize the outgoing electron distribution, it is sufficient to uniformly load the ions of interest into a box encompassing the focal volume. Then, by examining the correlation between final energy and initial position (or other classical S-matrix projections), more favorable distributions can be identified. In an experiment, there is no need to pre-form Ar^{16+} or Ar^{17+} in the focal volume. So long as any lower charge state of argon is present, and provided the main 10 PW pulse comes to a suitable focus, all higher charge states will be sequentially produced as the applied field increases. The use of a plasma lens to assist the focusing is addressed in section V.

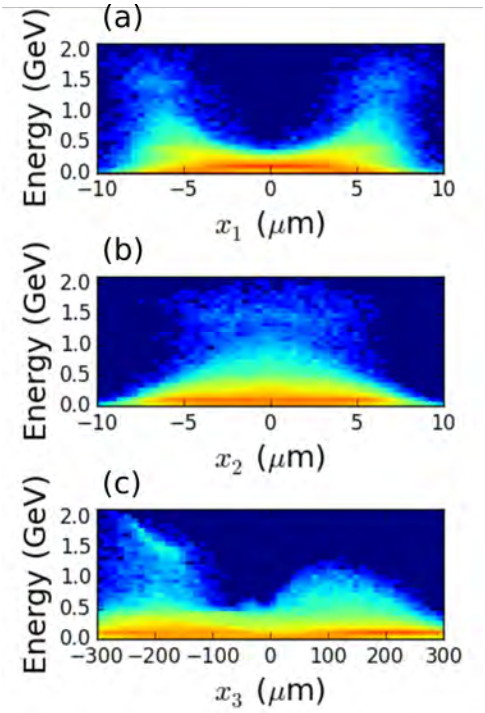

FIG. 4: Classical S-matrix projections for xLIPA electrons in the 10 PW case. The vertical axes are the final particle energies and the horizontal axes are the initial positions x_i, with laser polarization in the 1-direction and central wavevector in the 3-direction. High energies are encouraged by increasing the ion density near the two positions $(x_1, x_2, x_3) \approx (\pm 7, 0, -200)$ μm.

The electron distribution from a uniform background of Ar^{17+} is shown in Fig. 3. The momentum distribution is given in the three possible two-dimensional momentum planes. A strong preference for the polarization plane is indicated in Fig. 3(c), given that the color scale is logarithmic. The angle-energy plane is a promising experimental observable. A distinct population of high energy electrons can be seen around 1.5 GeV, at an angle of a few milliradians with respect to the laser propagation axis. In a separate simulation with the longitudinal field components artificially suppressed, the energy gain was about half that obtained with the longitudinal fields included.

It is possible to optimize the electron energy distribution by controlling the initial spatial distribution of the ions. In order to determine how to do this, a classical S-matrix is computed by correlating the initial and final states of a large number of particles. Projections of this S-matrix are shown in Fig. 4. In interpreting the figure, the limitations of two-dimensional plotting have to be taken into account. The mapping between the initial spatial

point (x_1, x_2, x_3) and the final energy is much closer to one-one than can be gleaned by inspection of any of the three projections. The only source of dispersion in the spectrum of particles originating from a single spatial point is the variability in the phase at the moment of ionization, which in turn is due to the fundamental statistical nature of quantum mechanics.

The optimal distribution of ions, based on Fig. 4, is the pair of points $(x_1, x_2, x_3) \approx (\pm 7, 0, -200)$ μm. An approximation of this would be a ring with diameter 14 μm, centered on the x_3 axis, and upstream of the laser focus by 200 μm. A further approximation of this would be a plasma lens, which has a natural density minimum on-axis, situated with the laser focus slightly beyond the lens exit plane. Thus, as mentioned above, a plasma lens has the fortuitous property of weighting the electron spectrum toward higher energies.

C. Electron Distributions at multi-Exawatt Scale

In this section, the focusing conditions are the same as in the 10 PW case discussed above, but the laser power is increased to 25 EW. This gives $a_0 = 5000$, which suggests, based on Table I and Fig. 2, that the K-shell of gold is a suitable source of electrons in this case. Although present day laser technology is far from producing 25 EW of power, it is interesting to investigate how the xLIPA mechanism scales, and whether unambiguous signatures of radiation reaction are obtained.

Consider first the case with radiation reaction neglected. The final electron distributions at 25 EW, analagous to the 10 PW distributions of Fig. 3, are shown in Fig. 5. The most obvious difference between the two cases is that the highest energy particles are on-axis, and the highest energy is about 70 GeV rather than 2 GeV. Linear scaling with a_0 would give 100 GeV, while the scaling of Eq. (11) would give 30 GeV.

The S-matrix projections at 25 EW, analagous to the 10 PW projections of Fig. 4, are shown in Fig. 6. While there are some similarities, a notable difference is that some high energy particles originate on-axis. This may be an indication that the simple plane wave analysis of section II holds more closely in the 25 EW case.

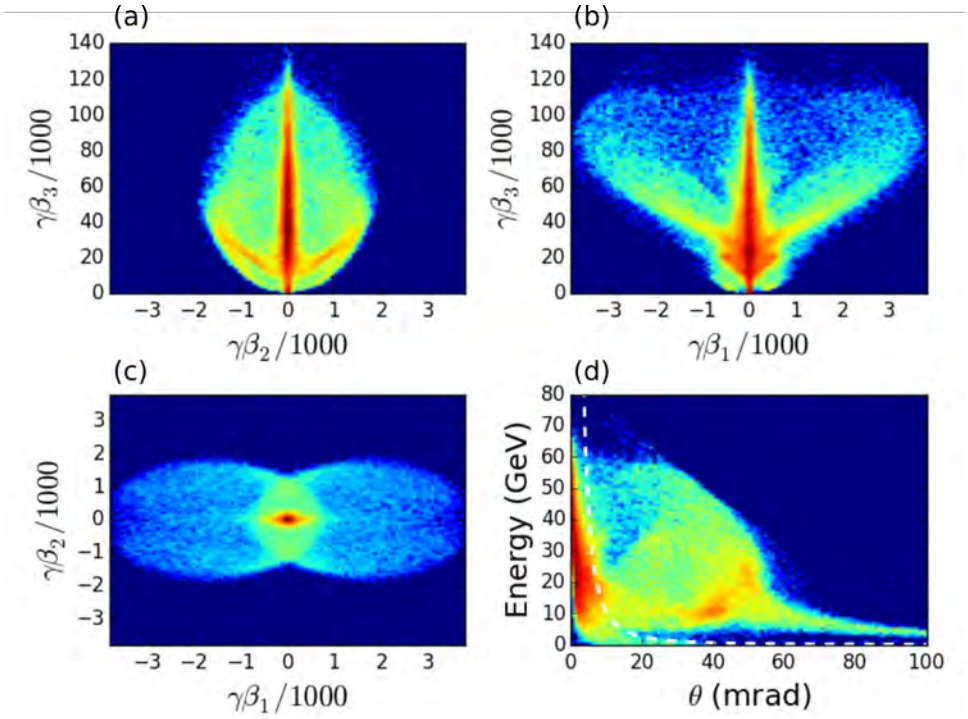

FIG. 5: Final distribution of electrons drawn from the K-shell of gold with 25 EW of laser power, neglecting radiation reaction. The momentum space distribution is shown in (a,b,c), and the angular-spectral distribution is shown in (d). $\gamma\beta_i$ is momentum normalized to mc, with laser polarization in the 1-direction and central wavevector in the 3-direction. The color scale is logarithmic. The dashed line in (d) is the curve on which all particles would lie in the plane-wave limit.

D. Radiation Reaction

Radiation reaction (RR) is one of the few areas of classical electrodynamics that is still lacking in experimental confirmation, mainly due to the lack of experimental facilities capable of accessing the radiation dominated regime. This issue has attracted significant attention in recent years [16–21]. The xLIPA process is a candidate for experimental observation of RR. In particular, if one can show that the angle-energy distribution is affected in a clear manner by RR, this might lead to a powerful confirmation, or denial, of the validity of the existing theories. The particle-tracking code used in this work has the option of including the Landau and Lifshitz RR formula [22]. It reproduces very closely the results reported in Ref. [21].

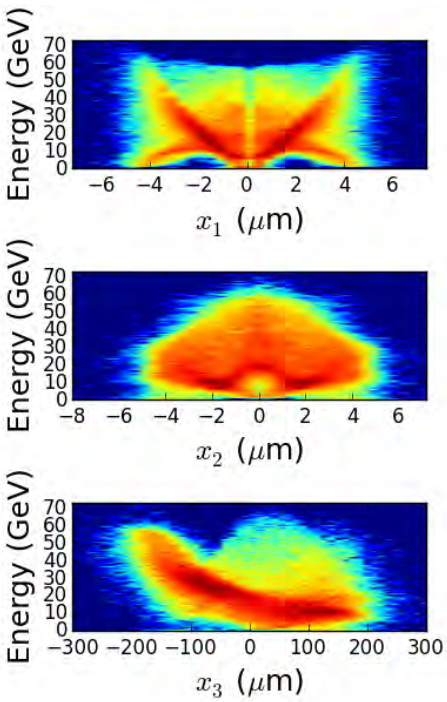

FIG. 6: Classical S-matrix projections for xLIPA electrons in the 25 EW case, neglecting radiation reaction. The vertical axes are the final particle energies and the horizontal axes are the initial positions x_i, with laser polarization in the 1-direction and central wavevector in the 3-direction. The vertical feature at $x_1 = 0$ in (a) is an artifact of the initial particle loading.

Before addressing the effect of RR on xLIPA, it is useful to consider the effect on the well-known solution for the motion of an electron in a plane-wave. This is illustrated in Fig. 7, for the case $a_0 = 1000$. Figs. 7(a,c,e) show the orbits neglecting RR, as computed by the particle-tracking code. The numerical error can be gauged by tracking the invariant, $\Upsilon \equiv u_0 - u_3$, which for the chosen initial conditions should be unity at all times. The observed error is less than 1%. Figs. 7(b,d,f) show the same orbits, except that RR is accounted for using the exact Landau and Lifshitz theory. The primary difference is that the formerly invariant Υ decreases at each turning point in the electron motion. This is consistent with expectations, since the turning points are where the acceleration, and hence radiated power, are greatest. Interestingly, a close look at Fig. 7(d) shows that u_3 reaches a higher value during the second half-cycle of the motion compared with the first. This implies that the energy also increases, since $u_0 = u_3 + \Upsilon$, and Υ changes only slightly. Naturally, energy need not be conserved in the presence of an external field.

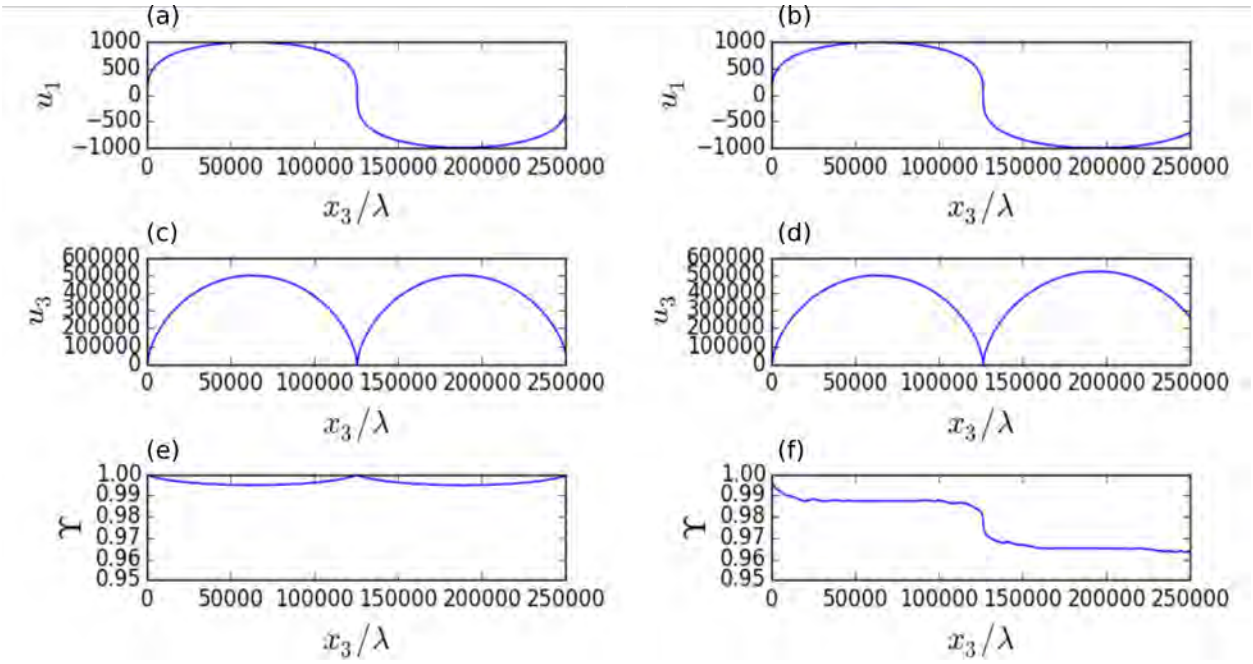

FIG. 7: Electron orbits in a plane wave without the reaction force (a,c,e) and with the exact Landau and Lifshitz reaction force (b,d,f). Here $\Upsilon = u_0 - u_3$, which is expected to be invariant in the absence of radiation reaction.

Fig. 8 shows a set of multi-EW xLIPA distributions with RR included. These should be compared with Fig. 5, which is an identical case with RR neglected. The overall effect of RR is to narrow the distributions, and to make the cutoffs more abrupt. Considering the log scale, Fig. 8(a) and (c) indicate that in the presence of RR, there are two fairly well defined beamlets with $u_2 \approx \pm 1000$ and $u_3 \approx 20000$. In the absence of RR these features become much more spread out in momentum space.

IV. NUMERICAL METHODS

The numerical model employed in this work incorporates a number of advances, including a covariant particle pusher that respects Lorentz invariance to machine precision, and elegantly incorporates radiation reaction and automatic time step adjustment. The ionization model uses the latest relativistic theories, and confines the use of the random number generator to the initial conditions. Finally, the implementation takes advantage of hardware acceleration by means of general purpose graphical processing units.

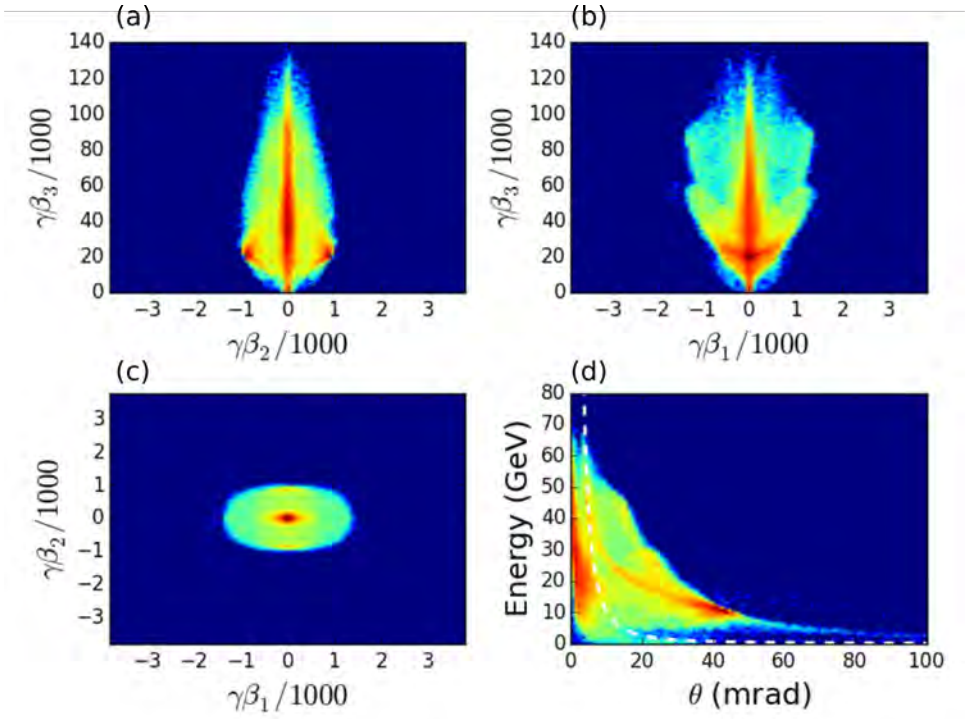

FIG. 8: Final distribution of electrons drawn from the K-shell of gold with 25 EW of laser power, including radiation reaction. The momentum space distribution is shown in (a,b,c), and the angular-spectral distribution is shown in (d). $\gamma\beta_i$ is momentum normalized to mc, with laser polarization in the 1-direction and central wavevector in the 3-direction. The color scale is logarithmic. The dashed line in (d) is the curve on which all particles would lie in the plane-wave limit, in the absence of RR.

A. Covariant Particle Pusher

The particle pusher calculates the world lines of particles introduced into the external field. Countless authors have implemented schemes for this purpose. One of the most commonly used schemes is the one introduced by Boris [23]. In carrying out simulations of laser-particle interactions, one most often chooses a time step that is some fixed fraction of the laser period. In the present case, this is not satisfactory because in the ultrarelativistic limit, there are turning points where the characteristic time scale is a very small fraction of the laser period. At the same time, one must propagate each particle to a point well outside the confocal region. These two requirements introduce a large scale separation, which demands some form of automatic time step adjustment. It turns out that this issue

can be resolved elegantly by designing the pusher to operate in covariant fashion, i.e., to push particles in proper time. In addition, a covariant particle pusher allows the exact Landau and Lifshitz radiation reaction formula to be incorporated in a simple way.

As in the Boris pusher, we choose to leapfrog momentum and position, except that these are now four-vectors, with the independent variable being proper time. The position equation can be updated trivially using

$$x(s + \Delta s) = x(s) + cu(s + \Delta s/2)\Delta s \tag{12}$$

where x and u are four-element column vectors. The matrix equation for the momentum is

$$\frac{du}{ds} = \Omega(s)u \tag{13}$$

where

$$\Omega(s) = \frac{q}{mc}\begin{pmatrix} 0 & E_x & E_y & E_z \\ E_x & 0 & B_x & -B_y \\ E_y & -B_x & 0 & B_z \\ E_z & B_y & -B_z & 0 \end{pmatrix} \tag{14}$$

Here, the fields $\mathbf{E}$ and $\mathbf{B}$ are considered functions of s. If they are prescribed as functions of the spacetime coordinates, as is typical, then one uses, e.g., the functional composition $\mathbf{E}(s) = \mathbf{E}(x) \circ x(s)$, where $x(s)$ is the solution of (12). Clearly, any valid Ω must be the generator of a Lorentz transformation, since $u^T u = 1$ is an identity.

Assume that the time step Δs is chosen to be small enough so that Ω is nearly constant. Then

$$u(s + \Delta s) = \Lambda(s + \Delta s/2, \Delta s)u(s) \tag{15}$$

where $\Lambda(s, \Delta s) = e^{\Omega(s)\Delta s}$. The matrix exponential of Ω is unwieldy, but can be greatly simplified by performing a decomposition between electric and magnetic fields. In particular, using the Campbell-Baker-Hausdorf expansion for the exponential of a sum, one obtains the preliminary result

$$\Lambda = \Lambda_E \Lambda_B \Lambda_{E\times B} + O(\Delta s^3) \tag{16}$$

where Λ_E is a boost, Λ_B is a rotation, and $\Lambda_{E\times B}$ is a boost that corrects for the fact that

boosts and rotations do not commute. More specifically,

$$\Lambda_E = \begin{pmatrix} 1-\chi & \psi\epsilon_1 & \psi\epsilon_2 & \psi\epsilon_3 \\ \psi\epsilon_1 & 1-\chi\epsilon_1^2 & -\epsilon_1\epsilon_2\chi & -\epsilon_1\epsilon_3\chi \\ \psi\epsilon_2 & -\epsilon_1\epsilon_2\chi & 1-\chi\epsilon_2^2 & -\epsilon_2\epsilon_3\chi \\ \psi\epsilon_3 & -\epsilon_1\epsilon_3\chi & -\epsilon_2\epsilon_3\chi & 1-\chi\epsilon_3^2 \end{pmatrix} \tag{17}$$

where $\chi = 1 - \cosh\beta$, $\psi = \sinh\beta$, $\beta = q|\mathbf{E}|\Delta s/mc$, and $\epsilon = \mathbf{E}/|\mathbf{E}|$, and

$$\Lambda_B = \begin{pmatrix} 1 & 0 & 0 & 0 \\ 0 & 1-\bar{\chi}(b_2^2+b_3^2) & b_1b_2\bar{\chi}+b_3\bar{\psi} & b_1b_3\bar{\chi}-b_2\bar{\psi} \\ 0 & b_1b_2\bar{\chi}-b_3\bar{\psi} & 1-\bar{\chi}(b_1^2+b_3^2) & b_2b_3\bar{\chi}+b_1\bar{\psi} \\ 0 & b_1b_3\bar{\chi}+b_2\bar{\psi} & b_2b_3\bar{\chi}-b_1\bar{\psi} & 1-\bar{\chi}(b_1^2+b_2^2) \end{pmatrix} \tag{18}$$

where $\bar{\chi} = 1 - \cos\theta$, $\bar{\psi} = \sin\theta$, $\theta = q|\mathbf{B}|\Delta s/mc$, and $b = \mathbf{B}/|\mathbf{B}|$. The $\Lambda_{E\times B}$ boost has the same form as Λ_E, with $\beta = q^2|\mathbf{E}\times\mathbf{B}|\Delta s^2/m^2c^2$ and $\epsilon = \mathbf{E}\times\mathbf{B}/|\mathbf{E}\times\mathbf{B}|$. However, it turns out that the explicit application of the correction $\Lambda_{E\times B}$ is not the most efficient way to achieve convergence. Instead, one can split the step in a manner similar to the Boris scheme to obtain

$$\Lambda(s,\Delta s) \approx \Lambda_E(s,\Delta s/2)\Lambda_B(s,\Delta s)\Lambda_E(s,\Delta s/2) \tag{19}$$

Based on a range of numerical experiments, this is significantly more accurate than (16).

In summary, updating u is a matter of carrying out three explicitly given linear transformations. The update is accurate to order Δs^2, and respects Lorentz invariance, i.e., $\Lambda^T g\Lambda = g$, to machine precision. One caveat is that the unit vectors are ill-defined in a field-free region. In practice, this is easily remedied, e.g., by superposition of a minuscule uniform field with the field of interest.

B. Timestep Adjustment, Accuracy and Performance

A useful feature of a covariant particle pusher is that a constant time step (in proper time) leads to a constant phase step for any particle in a plane wave. To see this, consider the total derivative of the phase

$$\frac{d\varphi}{ds} = \frac{d(k_\mu x^\mu)}{ds} = k_\mu \frac{dx^\mu}{ds} = k_\mu u^\mu \tag{20}$$

According to the exact solution of the equations of motion, $k_\mu u^\mu$ is invariant. Defining $\Upsilon \equiv k_\mu u^\mu/\omega$, and demanding the that phase step $\Delta\varphi \ll 2\pi$, one obtains the *necessary* accuracy condition

$$\Delta s \ll \frac{2\pi}{\omega\Upsilon} \tag{21}$$

which involves only invariant quantities. For a particle initially at rest, such as a tunnel ionized electron, one has $\Upsilon = 1$, so that the proper time step appropriate for a relativistic particle is the same as the lab frame time step appropriate for a non-relativistic particle. The reason for this is that the lab frame time step is longer than the proper time step by a factor of γ, which is just the right factor to keep the phase step constant. It should be noted that in cases where a laser pulse collides with an electron beam in a counter-propagating geometry, Υ can be large, requiring Δs to be correspondingly reduced.

The condition (21) alone is not sufficient to guarantee accuracy, because of the Campbell-Baker-Hausdorf expansion of the matrix exponential. In order to estimate the time step needed to justify truncation of the expansion, one may demand that $\Lambda_{E\times B}$ should be nearer the identity matrix than either Λ_E or Λ_B. Any of these matrices approach the identity as the angle (whether appearing in the argument of a hyperbolic or ordinary trigonometric function) vanishes. Therefore, demanding that the angle appearing in $\Lambda_{E\times B}$ should be much less than that appearing in Λ_E or Λ_B, provides the required accuracy condition. The overall result is

$$\Delta s \ll \min\left(\frac{2\pi}{\omega\Upsilon}, \frac{mc|\mathbf{E}|}{q|\mathbf{E}\times\mathbf{B}|}, \frac{mc|\mathbf{B}|}{q|\mathbf{E}\times\mathbf{B}|}\right) \tag{22}$$

As in the case of advancing the particle momentum, one has an undefined floating point operation in field-free regions. The remedy is again to add a minuscule uniform field

In practice it is convenient to have an expression for the timestep, Δs, not involving conditionals, and depending on a small number of dimensionless free parameters that quantify the desired accuracy. A suitable expression that is used in this work is

$$\Delta s = \left[\Omega^2\left(\frac{\omega\Upsilon}{2\pi}\right)^2 + \mathcal{R}^2\frac{q^2}{2m^2}\left(E^2+B^2\right)\right]^{-1/2} \tag{23}$$

The dimensionless free parameters are Ω, and $\mathcal{R}$, which can be thought of as frequency multipliers. The multiplier Ω corresponds to the number of steps taken during one period of the radiation field. The multiplier $\mathcal{R}$ accounts for the requirement due to non-commuting boost and rotation operators.

The effect of the parameter Ω is well known in connection with linear interactions, and does not require further exposition. The conservative value $\Omega = 267$ is used throughout this work. Fig. 9 illustrates the accuracy of the pusher in the case of a plane wave field with normalized vector potential $a(t, z) = a_0 \sin \omega(z - t)$. In the given scenario, $\Upsilon = 1$ is invariant, so that a suitable error measure is $|1 - \Upsilon|$, which should vanish at all time levels. The maximum value of the error measure during one period of the motion is shown as a function of $\mathcal{R}$, with $a_0 = 100$, in Fig. 9(a). Two-digit accuracy is only obtained for $\mathcal{R} \gtrsim 100$. Using a constant $\mathcal{R} = 1000$ and varying a_0 gives Fig. 9(b). In order to keep the accuracy fixed, one has to keep $\mathcal{R}/a_0$ approximately fixed. Available computation time sometimes dictates that higher accuracy is obtained for smaller a_0. For the simulations discussed in section III, we used $\mathcal{R}/a_0 = 10$ with $a_0 = 100$, and $\mathcal{R}/a_0 = 1$ with $a_0 = 5000$.

The covariant pusher described above is implemented as an OpenCL kernel. The performance under various conditions, running on an AMD D700 GPGPU, is illustrated in Fig. 10. The various points on the plot vary the number of particles involved in the calculation (horizontal axis), the floating point precision, and the number of particle advances per OpenCL kernel invocation. The latter parameter can be important because of the overhead involved in invoking the kernel, and also because of the cost of moving data in and out of cache at the beginning and end of the kernel invocation, respectively. In the best case, about 1.5 billion particles per second can be advanced, including field evaluations. The double precision

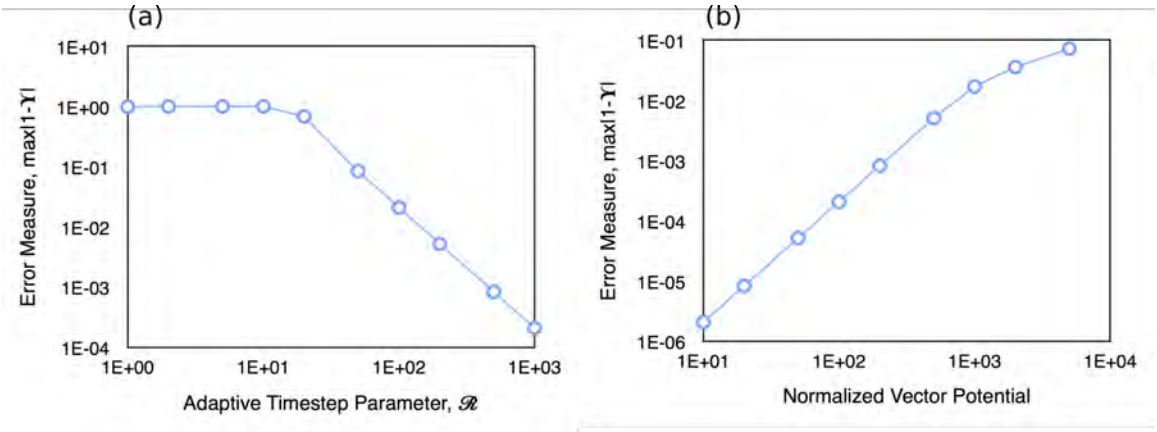

FIG. 9: Accuracy of covariant pusher, as measured by the maximum value of $|1 - \Upsilon|$, during one period of the motion of the electron in a plane wave. The accuracy is displayed as (a) a function of $\mathcal{R}$, given $a_0 = 100$, and (b) as a function of a_0, given $\mathcal{R} = 1000$. In all cases $\Omega = 267$.

performance is about 1/3 of this. The standard Boris pusher gives comparable performance.

C. Radiation Reaction

A major advantage of expressing the particle pusher in covariant fashion is that the Lorentz-Abraham-Dirac (LAD) formula for the radiation reaction force takes the simple form

$$R = \frac{2q^2}{3mc}\left(\frac{d^2u}{ds^2} - uu^T g\frac{d^2u}{ds^2}\right) \tag{24}$$

The Landau and Lifshitz (LL) formula is derived by substituting for d^2u/ds^2 the value obtained in the absence of radiation reaction. In three dimensional notation, the LL formula is extremely unwieldy, and even in four dimensional form, it *appears* to require expensive evaulations of all spacetime derivatives of the field tensor. When the covariant pusher described above is used, a simple and elegant alternative becomes readily available. Namely, by splitting each step into two half-steps, d^2u/ds^2 can be evaluated by direct finite differencing. That is, during each step generate

$$u^{(1)} = \Lambda\left(s + \frac{\Delta s}{4}, \frac{\Delta s}{2}\right)u^{(0)} \tag{25}$$

$$u^{(2)} = \Lambda\left(s + \frac{3\Delta s}{4}, \frac{\Delta s}{2}\right)u^{(1)} \tag{26}$$

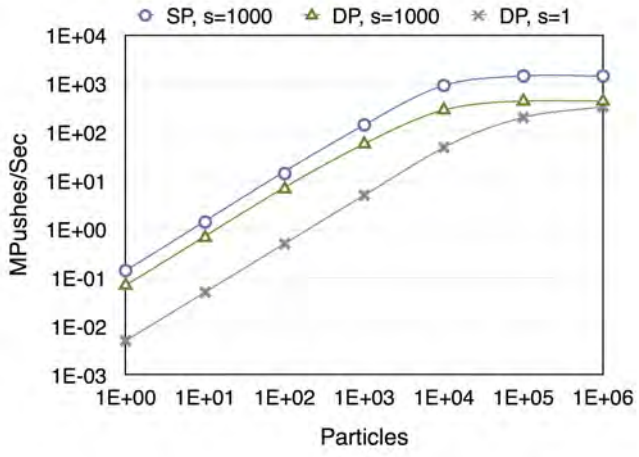

FIG. 10: Performance of covariant pusher, in terms of millions of particles advanced per second, including field evaluations. In the legend, SP means single precision, DP means double precision, and s is the number of cycles advanced for each OpenCL kernel invocation.

This requires field evaluations at only two spacetime points. Now, in the absence of radiation reaction, $u^{(0)} = u(s)$, $u^{(1)} = u(s + \Delta s/2)$, and $u^{(2)} = u(s + \Delta s)$. The LL reaction force is therefore given by the matrix equation

$$R = \frac{2q^2}{3mc}\left(\delta^2 u - uu^T g\delta^2 u\right) \tag{27}$$

where

$$\delta^2 u = \frac{u^{(2)} - 2u^{(1)} + u^{(0)}}{\Delta s^2/4} \tag{28}$$

is the finite difference form of d^2u/ds^2. The updated four-velocity, including the LL reaction force, is

$$u(s + \Delta s) = u^{(2)} + R\Delta s \tag{29}$$

Here, a simple Euler advance is justified by the expectation that the reaction force is small.

D. Ionization Algorithm

In the context of a classical particle tracking calculation, an ionization algorithm amounts to devising a rule for spawning a particle in the midst of the interaction. If the ion motion is negligible on the time scale of the laser pulse, an equivalent view is that the ionization algorithm provides a rule for abruptly changing the charge of a particle in the midst of the interaction. In particular, the electron charge is changed from $q = 0$ to $q = -e$ during one time step.

In order to avoid calling a random number generator while integrating the equations of motion (as is often done), we associate with each particle a constant parameter H, and an evolving parameter $\eta(t)$, which encode all the statistical information about the ionization process. The condition for a particle to be ionized is $\eta(t) > H$. The parameter H appears in the initial distribution function

$$g(x, p, H) = f(x, p)e^{-H} \tag{30}$$

where $f(x, p)$ is the usual phase space distribution. Let

$$\eta(t) = \int_{-\infty}^{t} w(t')dt \tag{31}$$

where $w(t)$ is the ionization rate evaluated for a given particle, which has to be computed using one of several available tunneling theories. These usually have the form

$$w(t) = C_1 E(t)^{C_2} \exp[-C_3/E(t)] \tag{32}$$

where $C_{1,2,3}$ are constants that depend on the ionization potential, and perhaps other fixed parameters. Using the ionization condition $\eta(t) > H$, one obtains for the density of ionized particles

$$n(x,t) = \int dp \int_0^{\eta(t)} g(x,p,H) dH \tag{33}$$

where it is assumed the momentum of unionized particles is negligible. Carrying out the integration,

$$n(x,t) = n_0(x) \left[1 - e^{-\eta(t)}\right] \tag{34}$$

where $n_0(x)$ is the initial density of unionized particles. Upon differentiation with respect to time,

$$\frac{dn}{dt} = w(t) \left[n_0 - n(t)\right] \tag{35}$$

which is the correct macroscopic ionization rate, under the stated assumptions.

V. NONLINEAR PROPAGATION IN A PLASMA LENS

A laser pulse propagating in plasma acquires a phase proportional to the plasma density. Plasma with density variation imparts a spatially varying phase, causing the pulse to refract. Thus with appropriate spatial structuring the plasma can, in principle, be made to mimic any linear, solid-state optical element. Plasma-based optical elements, being already ionized, have the advantage of higher damage thresholds, allowing their use at higher intensities than solid-state elements. Furthermore, plasma optics can be cheaply and rapidly replaced, for instance, at the rep-rate of a gas jet or capillary [24, 25], or flow rate of a water jet [26].

A plasma lens, in which the density profile of the plasma increases quadratically with radius, can have enormous focusing power [11, 13]. For a density profile of the form $n_e = n_0 + \frac{1}{2} n_0'' r^2$, a short plasma lens imparts a quadratic phase analogous to the phase applied by a thin lens. Specifically, $\phi = -i(2\Delta/k_0 w_m^4) r^2$, where Δ is the lens thickness, k_0 the pulse wavenumber, $w_m = (2/\pi r_e n_0'')^{1/4}$ describes the lens curvature, and r_e is the classical electron radius. For an incident pulse with spot size w_0 the effective $f\# = (1/8)(w_m^2/\Delta w_0)(k_0 w_m)^2$ provided $f\# > (\Delta/2w_0)$. As an example, we take $\lambda = 2\pi/k_0 = 800$ nm, $w_m = 15$ μm, $w_0 = 250$ μm and $\Delta = 0.5$ mm, and find $f\# = 3.1$.

A thick plasma lens can be considered a truncated plasma waveguide [11, 27]. For the density profile above, the plasma waveguide supports a transverse Gaussian mode of exp(-

1) field radius w_m. If $w_0 > w_m$, the pulse will undergo spot size oscillations, reaching a minimum of $w_{\min} \approx w_0(w_m/w_0)^2$ after a distance $z \approx \pi k_0 w_m^2/4$, with an effective $f\# = (1/4)(w_m/w_0)k_0 w_m$. For the same parameters as above, we find $f\# = 1.8$. For both thick and thin plasma lenses well-established formation techniques can be employed. For instance through the gas ionization, plasma heating, and hydrodynamic expansion driven by ≈ 100 ps Nd:YAG pulse focused onto a gas jet [24].

The plasma lens configurations described above are essentially truncated versions of the plasma channels that have demonstrated laser propagation over many Rayleigh lengths [25, 27], and have been employed in channel-guided laser wakefield accelerators [28]. At moderate beam powers, the focusing in these plasma channel lenses is primarily determined by the plasma density profile. At high beam powers, relativistic self-focusing enhances the focusing effect. A thin uniform plasma slab acts as a focusing lens if the laser power is above the critical power for relativistic self-focusing [10]. However, the focusing strength is dependent on radial and axial variations in the pulse intensity, which produces substantial aberrations that can significantly degrade the focusing quality.

Here we examine the use of a plasma lens to focus the 10 PW beamlines under construction at ELI-NP. Currently ELI plans to have two optical paths ending with either an $f\# \approx 3$ or $f\# \approx 20$ parabolic mirror. A plasma lens placed within the target chamber would allow added flexibility in the focal geometry. Additionally, the plasma lens could serve as a spatial filter and help counteract any main pulse expansion resulting from pre-pulse effects. While a plasma lens has a higher damage threshold than a solid-state lens, at the extreme intensities of ELI, plasma-based optics can still acquire aberrations from nonlinear modifications to the plasma density. As a result, neither the simple estimates for the $f\#$ provided above nor a weakly relativistic approach will suffice [11, 12]. Said differently, optimizing a plasma lens for ELI requires models that can capture highly nonlinear modifications to the plasma density.

We take a hierarchical approach to optimizing the plasma lens, using a combination of three models with a varying degree of approximation: a computationally rapid, nonlinear thin lens model based on the beam propagation method (BPM), ponderomotive guiding center (PGC) simulations based on the modified paraxial wave equation [29], and fully electromagnetic 3D particle-in-cell (PIC) simulations [30]. Our starting point is the thin lens BPM model, which allows rapid parameter scans. This model uses the fully nonlinear plasma

density perturbation in the adiabatic limit: $\omega_p \tau_{\rm FWHM} > 1$, where $\omega_p = (4\pi e^2 n_0/m_e)^{1/2}$ is the plasma frequency and $\tau_{\rm FWHM}$ is the full-width at half-maximum (FWHM) duration of the laser pulse [31]. If the plasma lens is thin, $f\# > (\Delta/2w_0)$, the laser pulse acquires a phase

$$\phi = -i\frac{\Delta}{2k_0\gamma}\left[k_{p0}^2 + \frac{4}{w_m^4}r^2 + \nabla_\perp^2\gamma\right] \tag{36}$$

on passing through the lens, where $\gamma = (1 + |\mathbf{a}_\perp|^2/2)^{1/2}$ and $\mathbf{a}_\perp = e\mathbf{A}_\perp/m_e c^2$ is the normalized, transverse vector potential of the pulse. The last term on the right hand side of Eq. (36) represents the transverse ponderomotive expulsion of electrons from the laser pulse path. The γ^{-1} coefficient includes the nonlinearity responsible for relativistic self-focusing in the weakly nonlinear limit, $|\mathbf{a}_\perp| < 1$. After applying this phase, we can find the pulse profile at any distance, modified by the nonlinear aberrations, using the beam propagation method.

The most important parameter for the phenomena discussed in the previous sections is the peak pulse intensity. We consider the ELI laser system and focal geometry with the following parameters: $\lambda = 800$ nm, $\tau_{\rm FWHM} = 30$ fs, pulse energy $U = 200$ J, $f\# \approx 20$, and final parabolic mirror diameter $D = 0.5$ m. By itself this system produces an intensity of 4×10^{21} W/cm^2. As we will see the plasma lens can focus to intensities far surpassing this. The remaining parameters for optimizing the peak intensity are the thin plasma lens linear focal length $f = (1/4)(k_0 w_m)^2(w_m^2/\Delta)$, the location of the plasma lens upstream from the unassisted focus, the plasma lens width for which we choose $\Delta = 0.5$ mm, and the background plasma density n_0. The plasma lens focusing power is independent of n_0, while the nonlinear phase associated with effects such as relativistic self-focusing is proportional to n_0. Consequently nonlinear aberrations can be mitigated without sacrificing focusing power by choosing the background density as small as possible. Here we use $n_0 = 10^{18}$ cm^{-3}. Our initial condition for the BPM model is a pulse incident on the plasma lens with the appropriate phase front curvature and amplitude acquired by the aforementioned ELI parabolic mirror.

Fig. 11 displays the peak intensity as a function of plasma lens location, vertical axis, and plasma lens linear focal length, horizontal axis, for linear, $\gamma \to 1$, and nonlinear lenses. In both the linear and nonlinear cases, the peak intensity can be increased by moving the plasma lens backwards (equivalent to making the lens larger) or by decreasing the focal length, consistent with linear optics. Even with the nonlinear aberrations, the plasma lens

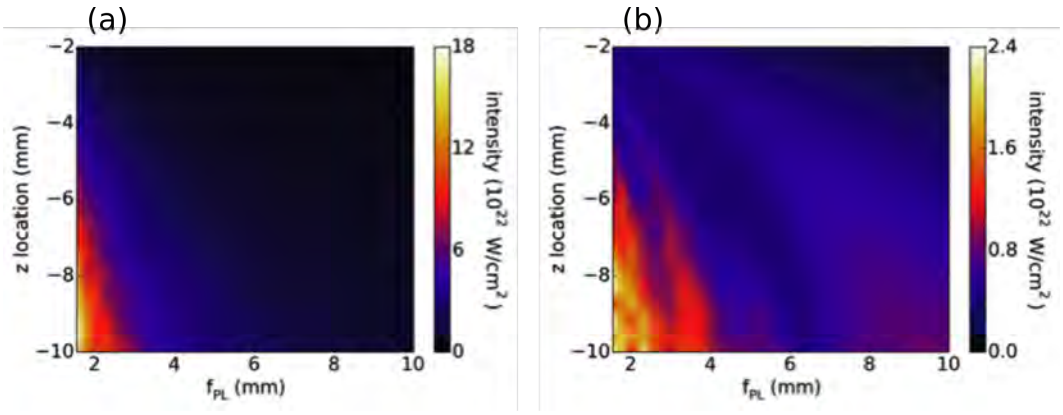

FIG. 11: Peak intensity as a function of plasma lens location, vertical axis, and plasma lens linear focal length, horizontal axis, for linear, $\gamma \to 1$, and nonlinear lenses. Even with the nonlinear aberrations, the peak intensity achieved by the plasma lens, $\approx 2 \times 10^{22}$ W/cm^2, surpasses that of the unassisted mirror, $\approx 4 \times 10^{21}$ W/cm^2.

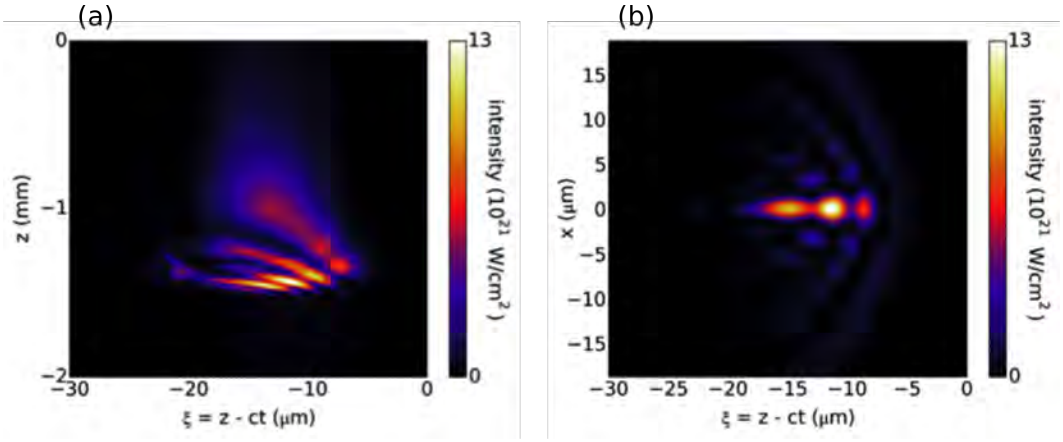

FIG. 12: (a) On-axis intensity as a function of distance in the speed of light frame, horizontal axis, and propagation distance, vertical axis. (b) The transverse intensity profile of the pulse at a propagation distance near where the pulse achieves its maximum intensity.

achieves a peak intensity ≈ 5 times greater than the unassisted focus.

To examine the focusing more closely, we performed a PGC simulation of the plasma lens focusing [29]. While these simulations take longer than the BPM, they capture the dynamic response of the plasma lens and the non-zero lens thickness. The same initial conditions described above were simulated with a plasma lens of focal length 0.45 mm located 2 mm upstream from the unassisted focus. The laser pulse was initialized with a $\sin^2$ temporal

profile. Even at this distance back from the unassisted focus, the normalized vector potential is already a sizable $|\mathbf{a}_\perp|_{\rm peak} = 8.7$.

Fig. 12(a) displays the on-axis intensity as a function of distance in the speed of light frame, horizontal axis, and propagation distance, vertical axis. The pulse reaches a peak intensity of 1.3×10^{22} W/cm^2: an intensity sufficient to ionize hydrogen-like argon or titanium and $\approx$ 4 times greater than the unassisted focal intensity. The multiple bright spots in Fig. 12(a) result from time slices within the pulse focusing at different axial locations owing to the varying degree of nonlinearity encountered. The center of the pulse has higher power than the front of the pulse, acquires a larger nonlinear modification to its phase, and focuses early. The back of the pulse, on the other hand, focuses even earlier having encountered the large ponderomotive electron density modification driven by the front of the pulse. Additionally, at a particular time slice, each transverse location converges to the optical axis at a different rate producing the swath-like features trailing the bright spots. Fig. 12(b) shows the transverse intensity profile of the pulse at a propagation distance near where the pulse achieves its maximum intensity. The brightest central spot corresponds to the center of the pulse at its peak intensity. The dimmer spots to the right and left correspond to the front and back of the pulse before and after their focuses respectively.

While these results are promising, the plasma lens focusing can be greatly improved. Our continuing research will focus on further optimization by modifying the plasma lens to correct for spherical aberrations resulting from the nonlinear laser-lens interaction, structuring the longitudinal profile of the lens, using leaky lenses for mode cleaning, and conducting full-format, 3D particle in cell simulations to examine non-cylindrically symmetry aberrations.

VI. RELATIVISTIC IONIZATION THEORIES

Studies of ionization of an atom in an electric field have a long history starting with experiments and analyses for the case of a constant electric field [32, 33]. A significant advance was made by Keldysh when he analyzed the case of a time-varying electric field [34]. Since then numerous analytical and numerical approaches have been employed with special emphasis on laser photoionization.

Besides interest in photoionization as a fundamental physical process there are many applications for photoelectrons. Knowledge of the electron properties, e.g., energy and

momentum distribution, is critical in some of these applications [4, 5].

Relativistic effects become significant either with increasing intensity or atomic number. An example of this is vacuum polarization whereby electron-positron pairs are created when the electric field approaches the Schwinger field. Photoionization of inner-shell electrons in high-Z atoms is another example where relativistic effects are important.

Two analytical approaches are prevalent in studies of photoionization. There are several interactions that must be incorporated in the analyses. The Coulomb interaction with the nucleus and the transition-inducing interaction with the electromagnetic field predominate. The imaginary time method (ITM) employs a Feynman propagator to evolve the final state from the initial bound state. The propagator is expressed as $e^{iS/\hbar}$, where $S = \int dtL$ is the action and L is the Lagrangian of an electron in a plane electromagnetic wave [35]. The action is written as a definite integral of L over time and the photoionization amplitude is given by minimizing the imaginary part of S using the classical orbits in the barrier region. In the second approach an exact S-matrix is defined as an overlap integral between a bound state in the distant past and a final state in the distant future [14, 36, 37]. Using the Klein-Gordon or the Dirac equations the overlap integrals are then re-written in the more familiar transition probability form involving the interaction inducing perturbation. The Volkov solution (electron wavefunction in the presence of an electromagnetic wave) plays a special role in the S-matrix approach.

A. Critique of Analytical Approaches

The analytical approaches for determination of ionization rate incorporate many approximations. Some of these are listed here.

1. Quasi-classicality

The quasi-classical nature of the main exponential factor, which is common to both approaches, requires that the barrier width measured along the direction of the electric field (i.e., the transverse axis of the figure-8 orbit), be large compared with the bound-state radius.

2. Gauge

The ITM employs the radiation gauge throughout. In analyses employing the S-matrix approach various gauges have been considered. However, different gauges lead to different results. The rationale for the choice of gauge has been discussed in Klaiber. It is known that ionization rates based on ITM are in good agreement with experimental results. Therefore it is argued that the appropriate gauge for the S-matrix approach is the one that recovers the ITM rates. This is the length gauge in non-relativistic theory which generalizes to the Göppert-Mayer gauge in relativistic theory. There is still the issue of partitioning the Hamiltonian operator into the bound-state Hamiltonian and the interaction Hamiltonian. The Coulomb-corrected dressed ionization rate corresponds to the choice where the bound-state Hamiltonian partially includes the electromagnetic field while the interaction Hamiltonian includes the remainder. The former takes into account the interaction of electron spin with the electromagnetic field due to i) bound-state energy level shifts (i.e., Zeeman splitting) and ii) electron spin precession in the laser field, while transition to the final state is due to the latter.

3. Nuclear Coulomb Tail

Except for negative ions (short-range potential) the nuclear charge has a significant effect on the wavefunction of the ejected electron and therefore on the ionization rate and is incorporated in both methods through a multiplicative factor. The approximations involved in analytical S-matrix approaches limit their validity to ionization potentials $\ll 0.5$ MV.

B. Ab Initio Simulations

In light of the limitations discussed above, an important part of the overall effort to describe a process such as xLIPA lies in benchmarking the ionization rate laws used in the particle tracking calculation. For this purpose NRL has developed a suite of ab initio simulation models which solve various quantum mechanical wave equations for a charged particle in an arbitrary electromagnetic field. The wave equations that have been incorporated into the suite are the Schrödinger, Pauli, Klein-Gordon, and Dirac equations. The entire suite of models takes advantage of a combined OpenCL/MPI programming model that scales to

large numbers of GPGPU devices operating in parallel. A subset of the models and results are documented in the literature [38–40].

VII. CONCLUSIONS

The xLIPA scheme of free space electron acceleration promises to produce highly directional, GeV class electrons, by means of direct acceleration in the fields of a multi-PW class laser pulse. In the process, nuclei of moderate-Z atoms such as argon or titanium are produced through tunneling ionization. The energy of the electrons, and charge of the nuclei, would be record-setting for free space acceleration and optical tunneling ionization, respectively. In the event that multi-EW laser pulses should become available, radiation reaction effects lead to observable effects in the momentum distribution. One way to reduce the laser power necessary for this is to improve the laser focus.

In order to improve the flexibility and efficacy of potential experimental configurations, a plasma lens is proposed as a combined final focusing element and target. In the linear approximation, the enhancement in irradiance due to the plasma lens may be orders of magnitude. When nonlinear effects are taken into account, lens aberrations limit the enhancement to factors of several. Investigations are underway to determine whether the aberrations can be corrected by tailoring the plasma lens density profile. In any case, the lens density profile weights the initial particle positions in favor of high final energy.

The xLIPA scheme has several benefits, both in terms of applications, and fundamental physics interest. One possible application is as an injector for a staged laser wakefield acceleration system. Another is as a source of high energy electrons to be used in driving an x-ray free electron laser, or other advanced light source. The fundamental physics of xLIPA is rich, consisting of relativistic tunneling ionization, charged particle dynamics in extreme fields, and eventually radiation reaction.

VIII. ACKNOWLEDGEMENTS

This work was supported by the NRL 6.1 Base Program. Helpful discussions with A. Zigler, J. Giuliani, A. Noble, K. Krushelnick, A. Maksimchuk, and J.R. Peñano are acknowledged. We are grateful to E. Turcu of ELI-NP for his encouraging response to this

topic, and the ELI-NP staff for hosting one of us (M.H.H.) on a site-visit.

[1] O. Tesileanu, D. Ursescu, R. Dabu, and N.V. Zamfir. Extreme light infrastructure - nuclear physics. *J. Phys.: Conf. Series*, 420:012157–1–012157–7, 2013.

[2] W.D. Kimura, G.H. Kim, R.D. Romea, L.C. Steinhauer, I.V. Pogorelsky, K.P. Kusche, R.C. Fernow, X. Wang, and Y. Liu. Laser acceleration of relativistic electrons using the inverse Cherenkov effect. *Phys. Rev. Lett.*, 74(4):546–549, Jan 1995.

[3] F.V. Hartemann, J.R. Van Meter, A.L. Troha, E.C. Landahl, N.C. Luhmann Jr., H.A. Baldis, A. Gupta, and A.K. Kerman. Three-dimensional relativistic electron scattering in an ultrahigh-intensity laser focus. *Phys. Rev. E*, 58(4):5001–5012, Oct 1998.

[4] C.I. Moore, A. Ting, S. McNaught, J. Qiu, H.R. Burris, and P. Sprangle. A laser-accelerator injector based on laser ionization and ponderomotive acceleration of electrons. *Phys. Rev. Lett.*, 82(8):1688–1691, 1999.

[5] C. I. Moore, A. Ting, T. Jones, E. Briscoe, B. Hafizi, R. F. Hubbard, and P. Sprangle. Measurements of energetic electrons from the high-intensity laser ionization of gases. *Phys. Plasmas*, 8(5):2481, May 2001.

[6] P.X. Wang, Y.K. Ho, X.Q. Yuan, Q. Kong, N. Cao, A.M. Sessler, E. Esarey, and Y. Nishida. Vacuum electron acceleration by an intense laser. *Appl. Phys. Lett.*, 78(15):2253–2255, Apr 2001.

[7] D.N. Gupta, N. Kant, D.E. Kim, and H. Suk. Electron acceleration to GeV energy by a radially polarized laser. *Phys. Lett. A*, 368:402–407, 2007.

[8] D. Cline, L. Shao, X. Ding, Y. Ho, Q. Kong, and P. Wang. First observation of acceleration of electrons by a laser in a vacuum. *J. Modern Phys.*, 4:1–6, 2013.

[9] R.B. Palmer. An introduction to acceleration mechanisms. Technical Report SLAC-PUB-4320, Stanford Linear Accelerator Center, May 1987.

[10] C. Ren, B.J. Duda, R.G. Hemker, W.B. Mori, T. Katsouleas, T.M. Antonsen, and P. Mora. Compresing and focusing a short laser pulse by a thin plasma lens. *Phys. Rev. E*, 63:026411, 2001.

[11] R.F. Hubbard, B. Hafizi, A. Ting, D. Kaganovich, P. Sprangle, and A. Zigler. High intensity focusing of laser pulses using a short plasma channel lens. *Phys. Plasmas*, 9(4):1431–1442, Apr 2002.

[12] B. Hafizi, A. Ting, R.F. Hubbard, P. Sprangle, and J.R. Peñano. Relativistic effects on intense laser beam propagation in plasma channels. *Phys. Plasmas*, 10(5):1483–1492, May 2003.

[13] Y. Katzir, S. Eisenmann, Y. Ferber, A. Zigler, and R.F. Hubbard. A plasma microlens for ultrashort high power lasers. *Appl. Phys. Lett.*, 95(3):031101–1–031101–3, 2009.

[14] M. Klaiber, E. Yakaboylu, and K.Z. Hatsagortsyan. Above-threshold ionization with highly charged ions in superstrong laser fields. II. Relativistic Coulomb-corrected strong-field approximation. *Phys. Rev. A*, 87:023418–1–023418–11, 2013.

[15] S. Augst, D. Strickland, D.D. Meyerhofer, S.L. Chin, and J.H. Eberly. Tunneling ionization of noble gases in a high-intensity laser field. *Phys. Rev. Lett.*, 63(20):2212–2215, Nov 1989.

[16] F. Rohrlich. Dynamics of a classical quasi-point charge. *Phys. Lett. A*, 303:307–310, 2002.

[17] F.V. Hartemann, D.J. Gibson, and A.K. Kerman. Classical theory of Compton scattering: Assessing the validity of the Dirac-Lorentz equation. *Phys. Rev. E*, 72:026502–1–026502–9, 2005.

[18] A. Di Piazza, K.Z. Hatsagortsyan, and C.H. Keitel. Strong signatures of radiation reaction below the radiation-dominated regime. *Phys. Rev. Lett.*, 102:254802–1–254802–4, 2009.

[19] A.G.R. Thomas, C.P. Ridgers, S.S. Bulanov, B.J. Griffin, and S.P.D. Mangles. Strong radiation-damping effects in a gamma-ray source generated by the interaction of a high-intensity laser with a wakefield-accelerated electron beam. *Phys. Rev. X*, 2:041004–1–041004–13, 2012.

[20] N. Kumar, K.Z. Hatsagortsyan, and C.H. Keitel. Radiation-reaction-force-induced nonlinear mixing of Raman sidebands of an ultraintense laser pulse in a plasma. *Phys. Rev. Lett.*, 111:105001–1–105001–5, 2013.

[21] Y. Kravets, A. Noble, and D. Jaroszynski. Radiation reaction effects on the interaction of an electron with an intense laser pulse. *Phys. Rev. E*, 88:011201–1–011201–5, 2013.

[22] L.D. Landau and E.M. Lifschitz. *Classical Theory of Fields*. Pergamon Press, Oxford, England, 1980.

[23] J. P. Verboncoeur. particle simulation of plasmas: review and advances. *Plasma Phys. and Control. Fusion*, 47:A231–A260, 2005.

[24] H. Sheng, K.Y. Kim, V. Kumarappan, B.D. Layer, and H.M. Milchberg. Plasma waveguides efficiently generated by Bessel beams in elongated cluster gas jets. *Phys. Rev. E*, 72(3):036411–1–036411–8, Sep 2005.

[25] D. Kaganovich, A. Ting, C.I. Moore, A. Zigler, H.R. Burris, Y. Ehrlich, R. Hubbard, and P. Sprangle. High efficiency guiding of terawatt subpicosecond laser pulses in a capillary discharge plasma channel. *Phys. Rev. E*, 59(5):4769–4772, May 1999.

[26] D. Panasenko, A. Shu, A. Gonsalves, K. Nakamura, N.H. Matlis, C. Toth, and W.P. Leemans. Demonstration of a plasma mirror based on a laminar flow water film. *J. Appl. Phys.*, 108(4):044913–1–044913–4, 2010.

[27] C.G. Durfee, III and H.M. Milchberg. Light pipe for high intensity laser pulses. *Phys. Rev. Lett.*, 71(15):2409–2412, Oct 1993.

[28] C.G.R. Geddes, C.S. Toth, J. van Tilborg, E. Esarey, C.B. Schroeder, D. Bruhwiler, C. Nieter, J. Cary, and W.P. Leemans. High quality electron beams from a plasma channel guided laser wakefield accelerator. *Nature*, 431:538–541, 2004.

[29] D.F. Gordon, W.B. Mori, and T.M. Antonsen, Jr. A ponderomotive guiding center particle-in-cell code for efficient modeling of laser plasma interactions. *IEEE Trans. Plasma Sci.*, 28(4):1224–1232, Aug 2000.

[30] D.F. Gordon. Improved ponderomotive guiding center algorithm. *IEEE Trans. Plasma Sci.*, 35(5):1486–1488, Oct 2007.

[31] Eric Esarey, Phillip Sprangle, Jonathan Krall, and Antonio Ting. Self-focusing and guiding of short laser pulses in ionizing gases and plasmas. *IEEE J. Quantum Electron.*, 33(11):1879–1914, Nov 1997.

[32] Y.P. Raizer. *Gas Discharge Physics*. Springer, 1991.

[33] L.D. Landau and E.M. Lifschitz. *Quantum Mechanics*. Pergamon Press, Oxford, England, 1980.

[34] L. V. Keldysh. Ionization in the field of a strong electromagnetic wave. *Soviet Physics JETP*, 20(5):1307–14, May 1965.

[35] V.S. Popov. Tunnel and multiphoton ionization of atoms and ions in a strong laser field (Keldysh theory). *Physics-Uspekhi*, 47(9):855–885, 2004.

[36] H.R. Reiss. Complete Keldysh theory and its limiting cases. *Phys. Rev. A*, 42(3):1476–1486, Aug 1990.

[37] H.R. Reiss. Theoretical methods in quantum optics: S-matrix and Keldysh techniques for strong-field processes. *Prog. Quant. Electr.*, 16:1, 1992.

[38] D.F. Gordon and B. Hafizi. Time dependent schroedinger equation on arbitrary structured

grids: application to photoionization. *J. Comp. Phys.*, 231:6349–6359, 2012.

[39] D.F. Gordon, B. Hafizi, and M.H. Helle. Solution of relativistic quantum optics problems using clusters of graphical processing units. *J. Comp. Phys.*, 267(15):50–62, Jun 2014.

[40] D.F. Gordon, B. Hafizi, and A.S. Landsman. Amplitude flux, probability flux, and gauge invariance in the finite volume scheme for the schroedinger equation. *J. Comp. Phys.*, 280:457–464, Jan 2015.

REPORT DOCUMENTATION PAGE

Form Approved
OMB No. 0704-0188

1. REPORT DATE *(DD-MM-YYYY)*	**2. REPORT TYPE**	**3. DATES COVERED** *(From - To)*
19-08-2015	Interim	May 2014 – May 2015

4. TITLE AND SUBTITLE

xLIPA: Promotion of Electrons from the K-shell to 2 GeV using 10 PW Laser Pulses

5a. CONTRACT NUMBER

5b. GRANT NUMBER

5c. PROGRAM ELEMENT NUMBER

6. AUTHOR(S)

D. Gordon, J. Palastro, B. Hafizi, D. Kaganovich, L. Johnson, R. Hubbard, M. Helle, A. Ting, and Y. Chen*

5d. PROJECT NUMBER
67-4987-05

5e. TASK NUMBER

5f. WORK UNIT NUMBER

7. PERFORMING ORGANIZATION NAME(S) AND ADDRESS(ES)

Naval Research Laboratory
4555 Overlook Avenue, SW
Washington, DC 20375-5320

8. PERFORMING ORGANIZATION REPORT NUMBER

NRL/MR/6791--15-9634

9. SPONSORING / MONITORING AGENCY NAME(S) AND ADDRESS(ES)

Naval Research Laboratory
4555 Overlook Avenue, SW
Washington, DC 20375-5320

10. SPONSOR / MONITOR'S ACRONYM(S)

NRL

11. SPONSOR / MONITOR'S REPORT NUMBER(S)

12. DISTRIBUTION / AVAILABILITY STATEMENT

Approved for public release; distribution is unlimited.

13. SUPPLEMENTARY NOTES

*Research Support Instruments, Inc., Lanham, MD 20706

14. ABSTRACT

Inner shell atomic electrons that are tunnel ionized in multi-petawatt class laser pulses are accelerated, in vacuum, to multi-GeV energies in the forward direction. In extreme fields, tunnel ionized electrons can be brought to the speed of light so abruptly, that they stay in the same phase of the laser field throughout significant portions of the confocal region. An analysis of the acceleration process is given, and relativistically covariant four-dimensional numerical calculations especially suited for extreme fields are carried out. Radiation reaction is included, and the latest relativistic tunneling ionization theories are used to spawn the simulated electrons. An experimental configuration is suggested, utilizing the 10 petawatt ELI-NP laser, and plasma lens assisted focusing.

15. SUBJECT TERMS
Laser Petawatt Acceleration
Ionization Exawatt

16. SECURITY CLASSIFICATION OF:			**17. LIMITATION OF ABSTRACT**	**18. NUMBER OF PAGES**	**19a. NAME OF RESPONSIBLE PERSON**
a. REPORT	**b. ABSTRACT**	**c. THIS PAGE**			Daniel F. Gordon
Unclassified Unlimited	Unclassified Unlimited	Unclassified Unlimited	Unclassified Unlimited	36	**19b. TELEPHONE NUMBER** *(include area code)* (202) 767-5036

Standard Form 298 (Rev. 8-98)
Prescribed by ANSI Std. Z39.18